Light scattering from deformed droplets and droplets with inclusions. I. Experimental results

David R. Secker, Paul H. Kaye, Richard S. Greenaway, Edwin Hirst, David L. Bartley, and Gorden Videen

We provide experimental results from the scattering of light by deformed liquid droplets and droplets with inclusions. The characterization of droplet deformation could lead to improved measurement of droplet size as measured by commercial aerodynamic particle-sizing instruments. The characterization of droplets with inclusions can be of importance in some industrial, occupational, and military aerosol monitoring situations. The nozzle assembly from a TSI Aerodynamic Particle Sizer was used to provide the accelerating flow conditions in which experimental data were recorded. A helium–neon laser was employed to generate the light-scattering data, and an externally triggered, pulsed copper vapor laser provided illumination for a droplet imaging system arranged orthogonal to the He–Ne scattering axis. The observed droplet deformation correlates well over a limited acceleration range with theoretical predictions derived from an analytical solution of the Navier–Stokes equation.

OCIS codes: 290.0290, 290.5820, 290.5850.

1. Introduction

We are currently investigating light-scattering methods that could be used to correct for errors that are known to occur in the measurement of liquid droplets by commercial aerodynamic particle-sizing instruments. During our investigation, it became apparent that the apparatus used for droplet deformation studies was also capable of reproducibly generating droplets with inclusions. These are of importance because they can be representative of aerosols found in a hospital or on a battlefield, where biological organisms can survive for prolonged periods when contained within a protective liquid coat. In this paper therefore we describe acquisition of experimental light-scattering data from both deformed droplets and droplets with inclusions. These data can be used to help develop and test theoretical inversion algorithms, some of which are described in part II of the paper,[1] which could ultimately allow rapid characterization and/or identification of these droplet morphologies. This in turn could lead to improvements in commercial aerodynamic particle sizers and new opportunities for the development of light-scattering aerosol monitoring instruments for bioaerosol detection.

A. Aerodynamic Particle Sizers

The size of an airborne droplet can be defined in a number of ways depending on the method of measurement. However, in studies of therapeutic aerosol sprays, combustion aerosols, paint sprays, and coatings, where on-line or real-time measurements are required or where the airborne behavior of the droplet is relevant to the application, the aerodynamic size d_a is frequently sought. d_a is defined as the diameter of a unit density sphere having the same gravitational-settling velocity as the particle in question. The traditional method of determining the aerodynamic size of a particle was by measurement of its gravitational-settling velocity with suitable sedimentation instruments. This process was slow and laborious, and commercial instruments based on the acceleration of particles were developed as an alternative.[2] The most widely used commercial aerodynamic sizers are the TSI Aerodynamic Particle Sizer (APS) family of instruments (3300 se-

D. R. Secker (d.r.secker@herts.ac.uk), P. H. Kaye, R. S. Greenaway, and E. Hirst are with the Science and Technology Research Centre, University of Hertfordshire, Hatfield AL10 9AB, UK. D. L. Bartley is with the National Institute for Occupational Safety and Health, Cincinnati, Ohio 45226. G. Videen (videen@atm.dal.ca) is with the U.S. Army Research Laboratory, 2800 Powder Mill Road, Adelphi, Maryland 20783-1197.

Received 10 January 2000; revised manuscript received 19 June 2000.

0003-6935/00/275023-08$15.00/0

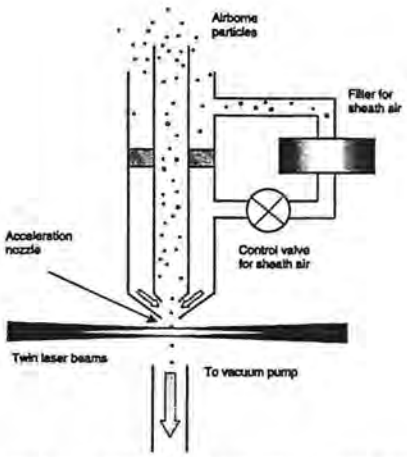

Fig. 1. Schematic diagram of the particle delivery system used in TSI APS 3300 series instruments.

ries, TSI Inc., St. Paul, Minn.), which achieve the desired particle size measurement by acceleration of a sample airstream in which the particles are suspended and by measurement of the velocity acquired by individual particles. The larger particles exhibit greater inertia and thus accelerate more slowly, thereby attaining lower velocities. In the APS instruments, an aerodynamic accelerating nozzle, in which a sample flow is sheathed in filtered air, produces the necessary accelerating flow, as illustrated in Fig. 1. The total airflow through the nozzle is regulated to 5 l/min, of which 4 l/min is filtered to provide the sheath flow. The time of flight of the particle through two closely spaced laser beams positioned a few hundred micrometers beneath the nozzle exit is recorded from the pulses of light scattered by the particle to an optical detector. An assessment of the particle's aerodynamic size is determined when the transit time is related to an internal calibration function based on measured times of flight of solid spherical calibration particles. The size range covered by this instrument is from 0.5- to 30-μm aerodynamic diameter, depending on the instrument model used.

However, aerodynamic sizing instruments of this type suffer a significant limitation in that the measured aerodynamic size can be significantly affected by particle shape. When one attempts to measure nonspherical particles of known density, the shape (and orientation) of each particle subjected to the accelerating airflow governs the drag force it experiences and hence affects the measured aerodynamic size. The measurement of liquid aerosol droplets is subject to significant error (25% undersizing reported in some cases) because the droplets deform to oblate spheroids in the accelerating airflow. As a result of this deformation, their cross-sectional area increases and they experience a greater acceleration than would be the case with similar-sized rigid spheres. Despite being well reported in the past by Baron[3] and Griffiths *et al.*,[4] there is as yet no systematic method of measuring the degree of deformation experienced by individual droplets in the instrument, and material-specific calibration curves, derived, for example, with gravitational-settling techniques, are invariably required.

B. Spatial Light Scattering

The spatial distribution of light scattered by a particle, also in certain texts referred to as the two-dimensional angular optical scattering pattern,[5] is a complex function of the size, shape, dielectric structure, and orientation of the particle, as well as of the properties of the illuminating radiation (wavelengths, polarization state). Analysis of the scattering pattern can provide a way to characterize the shape, orientation, and internal structure of the illuminated particle, and many researchers have exploited this property in various ways. Previous research by the authors[6] has explored the potential of scattering pattern analysis for particle shape and size classification and has demonstrated[7,8] how such techniques can be implemented in real-time airborne particle measurement systems designed for ambient aerosol characterization and asbestos fiber detection.

Scattering patterns can cover different scattering angle ranges depending on the light collection geometry used to acquire them. We recorded the examples shown in Fig. 2 (see figure caption for a description of particle types) by imaging the pattern of light scattered by individual particles onto an intensified charge-coupled device (ICCD) camera as the particles were carried by an airstream through a laser beam. The particle transition time through the beam was ~2 μs; in each case light scattered between 5° and 30° scattering angle, and throughout 360° of azimuth was captured as a 256 by 256 pixel image. The beam direction is perpendicular to the paper in the center of each image. Each white dot in the patterns corresponds to a single scattered photon, and the images thus represent photon distribution maps of several thousands to several tens of thousands of scattered photons. The images illustrate the wide variations these patterns can assume for different particle shapes and orientations. It was the potential of spatial light-scattering analysis for real-time particle shape characterization that initiated the fundamental study of droplet scattering reported here. It also underpins an ultimate aim of this research, namely, to provide an on-line optical means to correct for the errors in measured aerodynamic size caused by droplet deformation in instruments such as the APS 3300 series.

2. Apparatus

An apparatus was constructed that allowed the acquisition of both spatial scattering patterns and real images from individual droplets in the below 30-μm-size range as they traversed the measurement space below an APS 3320 sample delivery nozzle (donated by TSI Inc.). The apparatus is shown schematically in Fig. 3. As stated above, the actual TSI APS 3300 series of instruments incorporate two closely spaced cross-polarized beams and measure particle time of

Fig. 2. Examples of spatial light-scattering patterns from individual airborne particles. Top row, left to right: hematite ellipsoid, 2 μm; copper flake, ~5 μm; sodium chloride crystal; sodium chloride crystal. Bottom row, from left to right: asbestos fiber (crocidolite); irregular background particle; asbestos fiber (chrysotile); water droplet, ~9 μm in diameter.

flight between the beams. However, for the fundamental results reported here, we produced the spatial light-scattering pattern images using a single beam from a 633-nm 15-mW plane-polarized He–Ne laser (Model 05-LHP-151, Melles Griot Laser Group, Carlsbad, Calif.). Furthermore, although the normal operating flow rate of the TSI APS instrument is 5 l/min (comprising 1-l/min sample flow rate and 4 l/min of filtered sheath flow), we additionally observed droplet behavior over a range of flow conditions both less than and greater than the norm so as to gain a greater understanding of the morphological changes that take place.

A. Light-Scattering Pattern Acquisition

The beam from the He–Ne laser passes through a quarter-wave plate to render the light circularly polarized before it is focused through a cylindrical lens to produce a beam of elliptical cross section (approximately 1.2 mm by 100 μm) at the point of intersection with the sample airflow. Monodisperse droplets are generated into the sample flow with a vibrating orifice aerosol generator (VOAG) (TSI Inc.) as described below. As each droplet traverses the beam, light scattered in the forward direction between angles of 5° and 20° is imaged onto an intensified, asynchronously triggered ICCD camera (ICCD225, Photek, Ltd., East Sussex, UK). The lower angular limit is set by a beam stop, whereas the higher limit is set to avoid shadowing of the scattered light by the lower surface of the sample delivery nozzle. Images from the camera are digitized, displayed, and stored on a computer at a rate of several images per second for later analysis. A trigger signal for the acquisition of a scattering pattern by the camera is derived from a separate photomultiplier detector module which receives light scattered at a higher scattering angle than the camera, as indicated in Fig. 3. The rising and trailing edges of the signal from the photomultiplier detector, respectively, initiate and terminate the camera integration period, this being typically ~2-μs duration.

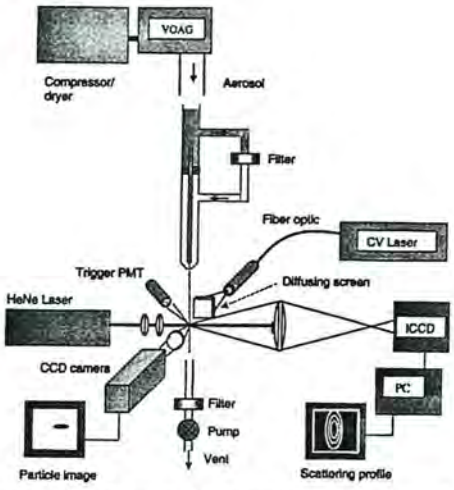

Fig. 3. Schematic diagram of apparatus used to acquire scattering patterns and real images from individual airborne droplets. PMT, photomultiplier tube; CV, copper vapor.

B. Droplet Image Acquisition

Real images of the droplets are acquired with a CCD camera assembly mounted orthogonal to the He–Ne scattering axis. In the manner first described by Baron[3] and Willeke and Baron,[9] the droplets are viewed against a bright diffusing screen. The illumination for this screen is derived from a copper vapor laser (Oxford Lasers, Ltd., UK) that delivers pulses of 38-ns duration at wavelengths of 510 and 578 nm. Each pulse has an energy of approximately 2 mJ. Again, appropriate triggering of the laser pulses is achieved by use of the signal from the pho-

tomultiplier detector. The imaging system uses a high numerical aperture microscope objective lens and a standard microscope tube, resulting in an overall image magnification of approximately ×10. A digital nonintensified CCD camera (Model KP-F100, Hitachi Denshi, Ltd., Tokyo, Japan) was used to acquire images because it has both high readout speed and small pixel size (6.7-μm square). This pixel size produced images of acceptable resolution, the diameter of a 20-μm droplet, for example, covers approximately 30 pixels within a 1300 × 1030 pixel image. A Foucault knife-edge test[10] was performed to determine the resolution of three pixels for the image quality attainable with this configuration.

It was originally intended to acquire scattering patterns and real images simultaneously from the same droplet. This would have required appropriate optical filtering to prevent the intense illumination from the copper vapor laser reaching the ICCD camera. However, because the pulsed radiation was broad field (as a result of the diffusion screen) and multiwavelength, the task of attenuating this radiation to a degree sufficient to prevent damage to the ICCD camera was extremely difficult without also significantly attenuating the 633-nm scatter light flux. Fortuitously, the uniformity of droplet size produced by the VOAG for a given set of generating conditions was such that the scattering patterns and images from successive droplets were remarkably reproducible, the differences being principally a result of the optical quantization noise. We therefore decided to avoid potential overillumination of the ICCD by recording the scattering patterns and real droplet images from successive droplets rather than the same droplet, ensuring that the ICCD was disabled during the firing of the pulsed laser.

C. Droplet Generation and Delivery

The VOAG produces droplets by inducing mechanical instability in a fine liquid jet through excitation with a piezoelectric oscillator. When first formed, droplets are comparatively large and comprise a solute, in our case either oleic acid or glycerol, in solution with an analytical reagent-grade isopropyl alcohol. Dry [<1% relative humidity (RH)] compressed air is used to transport the droplet aerosol from the VOAG drying column to the light-scattering instrument, during which time the alcohol evaporates to leave pure oleic acid or glycerol droplets. A bleed valve controls the total flow rate through the nozzle subsystem. For the experiments described, the total flow rate was set prior to the acquisition of scattering data, and the sheath airflow rate was measured prior to and during acquisition with a bubble flowmeter. The measured sample flow rate was found to be consistently 20% of the total flow rate and was found to be stable to within 1% during the period of experimental data acquisition.

3. Experimental Data

All experimental data presented here were recorded from oleic acid droplets, with the exception of that shown in Fig. 8(b) which shows scattering from a glycerin droplet. Figure 4 illustrates the changes that occur in the spatial light-scattering patterns from individual droplets as a function of both droplet size and increasing sample flow rate. Each scattering pattern was recorded over a 2-μs period as the droplet traversed the He–Ne beam beneath the aerosol delivery nozzle. Each scattering pattern therefore represents the forward scattering from deformed droplets illuminated at 90° to its axis of symmetry. The images on the top row of Fig. 4 were recorded from 8-μm-diameter droplets at total flow rates from 1 to 6 l/min, respectively. Subsequent rows show the scattering behavior of 12-, 16-, 20-, 25-, and 30-μm-diameter droplets for similar values of flow rate. The gain of the image intensifier was reduced for larger droplet sizes (and lower droplet velocities) to minimize optical saturation effects, although these are still present as extended solid white areas in some of the larger droplet and lower velocity patterns. Ananth and Wilson[11] have carried out a theoretical analysis of the gas and particle velocities present in the APS delivery nozzle. Their results predict that at the normal APS operational flow rate of 5 l/min, the gas velocity at the measurement point is approximately 160 m/s and the velocity of a 10-μm spherical particle is approximately 50 m/s.

At the lowest flow rate and smallest droplet size (top-left image), the scattering pattern correlates closely with that predicted by Mie theory[12] for a perfect sphere. No droplet deformation is discernible from the light-scattering data in this image. For increasing flow rate or droplet size, however, the degree of droplet deformation is evident from the increasing ellipticity of the scattering maxima and minima that are evident on the patterns. This behavior appears well behaved until a point is reached such as that shown by the image, 16-μm diameter and 5 l/min in Fig. 4, at which bright horizontal barring occurs on the image. This is predicted by the theoretical analysis described in part II of this paper.[1] This barring can occur either as a predominant central white bar or as a series of parallel horizontal scattering fringes as shown by the 20-μm diameter and 5 l/min image. An increase of the flow rate or droplet size further results in more-complex interference patterns within the images, such as can be seen in the image 30-μm diameter and 5 l/min. This behavior appears to indicate that the droplets are undergoing a transition from a simple oblate spheroidal form to the more-complex morphologies as first observed by Baron.[3] It also indicates that our task of attempting to assess the deformation of a single droplet rapidly by analysis of its light-scattering pattern (as we desire for on-line correction of deformation effects in aerodynamic sizing) is nontrivial for droplets deformed beyond a certain degree.

Figure 5 shows light-scattering pattern images for undistorted droplet diameters of 20, 25, and 30 μm and total flow rates from 1 to 6 l/min. Adjacent to each scattering pattern is the corresponding droplet image. These latter images indicate the changes in

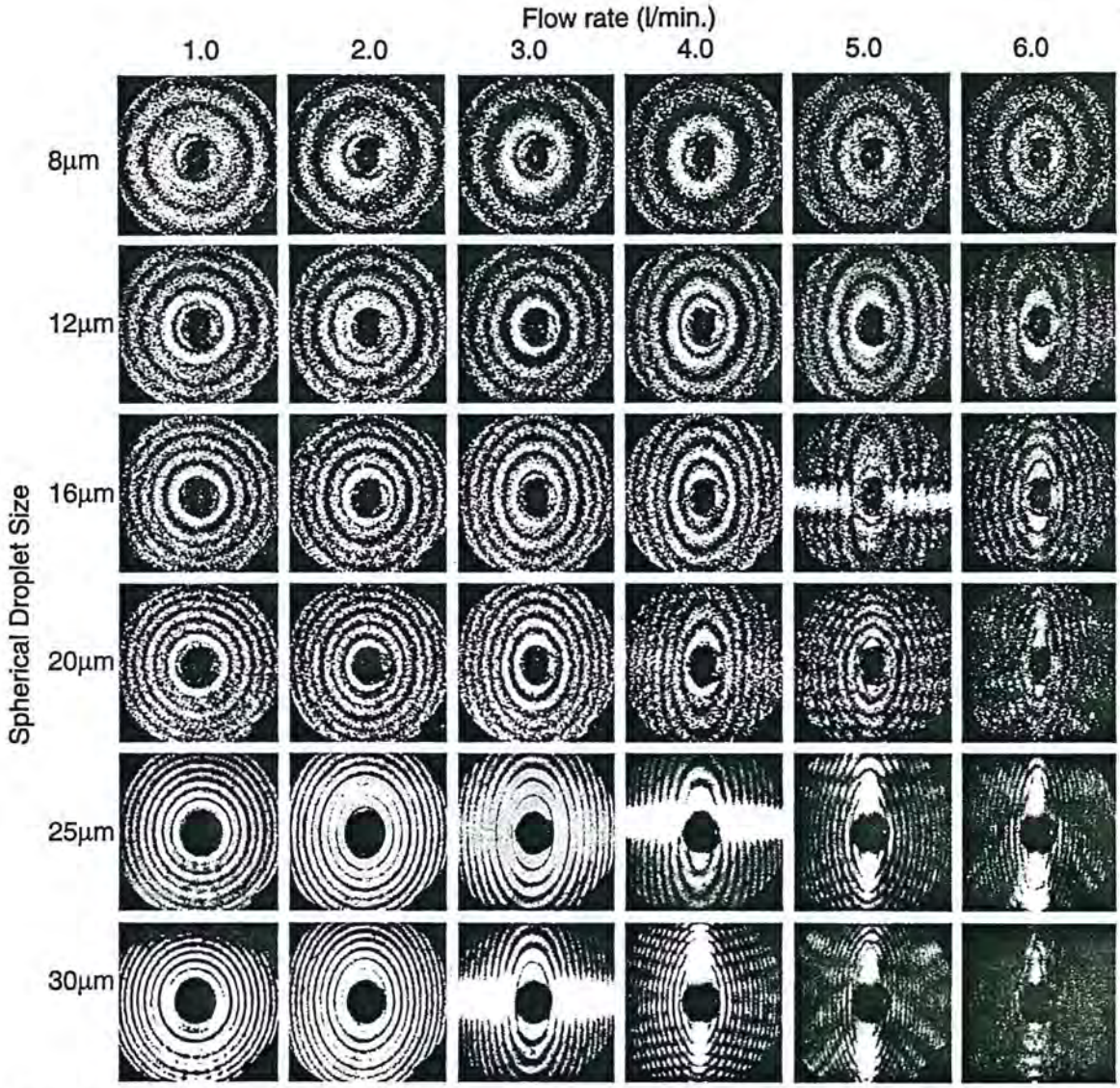

Fig. 4. Spatial light-scattering patterns from individual droplets as a function of droplet size and sample flow rate.

droplet shape that produce the increasingly complex scattering data. The essentially perfect spheres undergo flattening into oblate spheroids, then become biconcave disks before forming menisci having concave upper surfaces. This morphological transition coincides with the dominant feature of the respective scattering patterns changing from a horizontal to a vertical bright band, the former possibly the result of a morphology-dependent resonance in the droplet and the latter a function of the increasingly narrow horizontal cross section that the droplet presents. We are currently investigating these effects further with the hope of elucidating the causes of the dominant scattering features.

4. Quantifying Droplet Deformation

Inversion of the light-scattering data to yield droplet deformation descriptors is discussed in part II of this paper.[1] As a comparative measure, a first-order estimate of droplet deformation under given flow conditions can be obtained from the Feret ratio of the droplet image, defined as the ratio of Feret diameters, which are the maximum distances between particle edges in the x and y directions of the image (i.e., orthogonal to and parallel to the particle trajectory, respectively). The edges of the droplets $E(x, y)$ were determined by a computer-based Gaussian edge detection algorithm.[13] The threshold value for this algorithm can be set manually or left to be determined automatically from the background intensity. Because the background intensity is different for each image, the automatic threshold function was employed. In addition, the graininess of the background can make the algorithm detect erroneous edges in the background. However, the algorithm generally provides a continuous line that is evident as an edge in the binary file that the algorithm creates. The Feret ratio can then be determined from this binary file. Figure 6 shows a plot of the Feret ratio versus the flow rate for 20-μm oleic acid droplets.

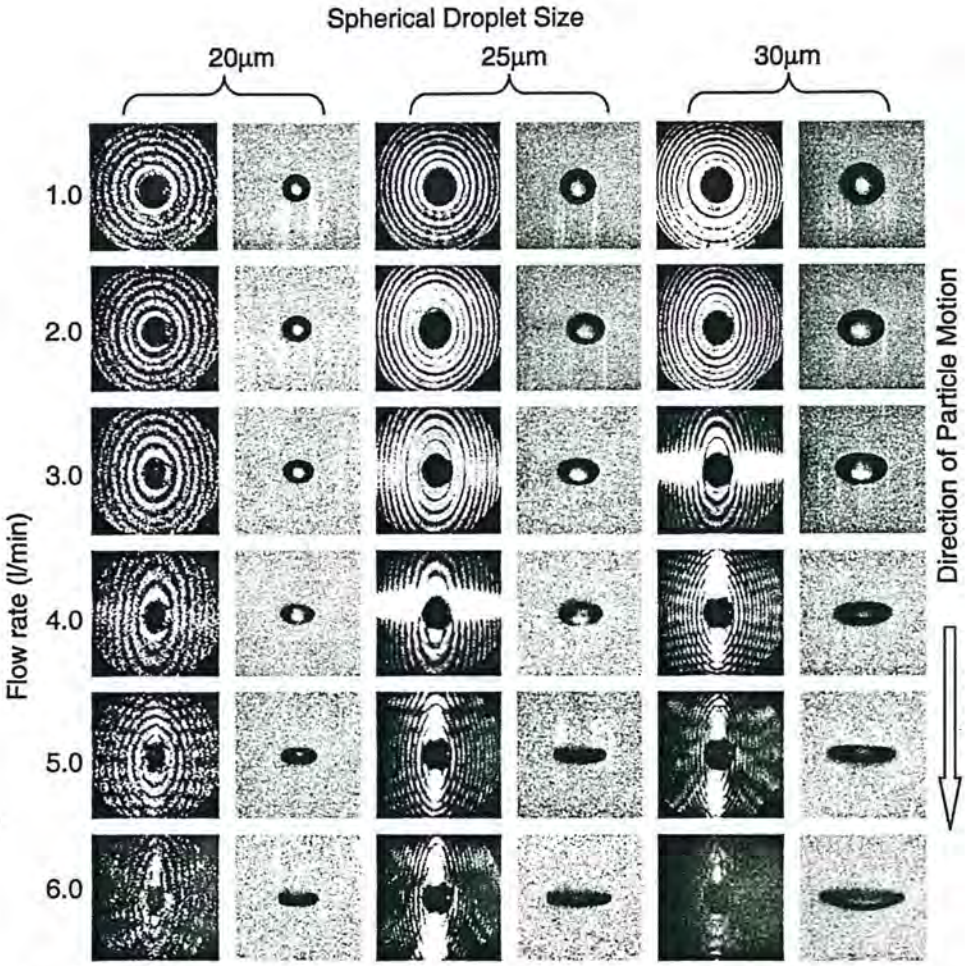

Fig. 5. Spatial light-scattering patterns and droplet images for 20-, 25-, and 30-μm-diameter droplets at various sample flow rates through the APS aerosol delivery nozzle.

As can be seen in the figure, the Feret ratio is well behaved up to the 4.5-l/min flow rate. The reduction in the rate of increase of the Feret ratio immediately after this point coincides with the droplet beginning to assume a meniscus form (see Fig. 5), for which the Feret ratio is less. The change in the curve at the 4.5-l/min flow rate coincides with the point at which the horizontal banding appears in the scattering pattern. A significant part of the experimental uncertainty in the Feret ratio measurements is caused by blurring of the droplet images in the direction of motion, especially at higher flow rates. Methods to minimize motion blur by a reduction in the laser pulse width are currently being explored.

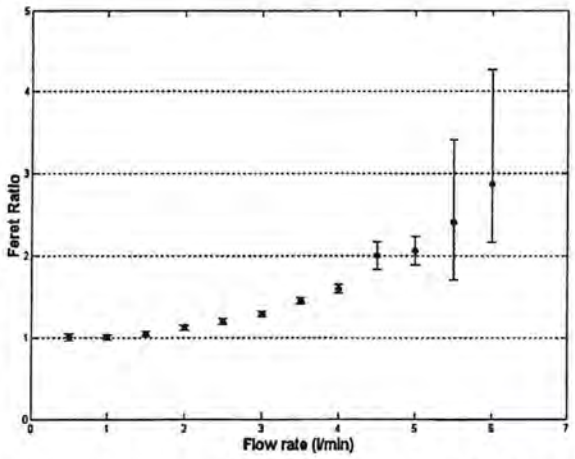

Fig. 6. Feret ratio plotted as a function of flow rate for 20-μm oleic acid droplets.

Liquid droplet distortion produced in an accelerating flow field has been computed through an analytical solution of the Navier–Stokes equation by Bartley *et al.*,[14] and this has led to a means of correlating observed droplet deformation to parameters such as droplet diameter, viscosity, surface tension, and density. A high Reynolds number empirical approximation to the pressure external to the droplet has been used in these calculations. This procedure, described in detail by Bartley *et al.*, correctly predicts the change in droplet shape with increasing flow rate from spherical to spheroidal to biconcave disk. For example, Fig. 7 shows the image of a 20-μm nominal diameter oleic acid droplet together with the corresponding computed cross section. Beyond this level

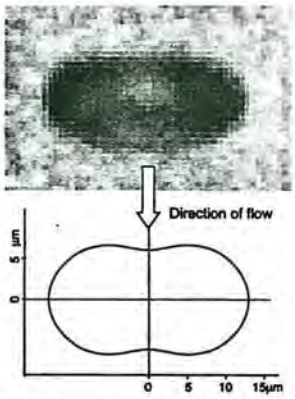

Fig. 7. Image of a 20-μm nominal diameter oleic acid droplet together with the corresponding computed cross-sectional shape. The computation used the following values: density, 0.90 g/cm^3; viscosity, 0.256 P; surface tension, 32 mJ/m^2.

of distortion, the theoretically computed shape pattern is not reliable.

5. Droplets with Inclusions

During the process of collecting experimental light-scattering and particle image data of the type described above, a phenomenon was observed that has since been attributed to the presence of inclusions in the observed liquid droplets. This is of potential interest because droplets with internal bodies can occur in environments such as hospital buildings where entities such as biological organisms can remain viable over long periods by encapsulation within liquids. Similar conditions can apply in the dispersal of biological warfare agents. As a consequence, there is interest in the theoretical modeling of light-scattering behavior of such two-component droplets, the object of which is ultimately to establish a way to recognize their presence in an environment. Reproducible experimental data from droplets with inclusions can thus provide a valuable resource to verify theoretical inversion methods.

As stated above, the VOAG droplets are normally generated into a dry atmosphere, typically <1% RH. When 20-μm droplets of glycerin, in which water is soluble, were generated into a moist atmosphere at 40% RH, no perturbations of the expected scattering patterns were observed [see Fig. 8(a)]. However, when similar-sized droplets of oleic acid, in which water is insoluble, were generated into the same atmosphere, light-scattering patterns of the type shown in Fig. 8(b) were consistently observed. These preliminary scattering data were recorded at a flow rate of 1 l/min.

The striking feature of the oleic acid pattern is the displaced secondary scattering fringes superimposed on the normal concentric rings from a homogeneous sphere. Figure 8(c) shows a droplet image from the same oleic acid aerosol [although, for the reasons given in Subsection 2.B., it is not from the same droplet as Fig. 8(b)], and this clearly shows the presence of an internal dielectric discontinuity. The position of

Fig. 8. Scattering patterns recorded from droplets generated in a 40% RH environment: (a) a 20-μm-diameter glycerin droplet with no inclusion and (b) a 20-μm oleic acid droplet with inclusion. (c) shows an image of the type of droplet giving rise to the scattering in (b).

the secondary scattering fringes relative to those from the host droplet provides good evidence to support the hypothesis of an inclusion offset vertically upward from the center of the oleic acid host, and again this is supported both by the reproducibility of the images of the droplets [such as Fig. 8(c)] and by theoretical analysis.[1] The cause of this upward shift of the inclusion within the host may reasonably be assumed to be due to the density difference between

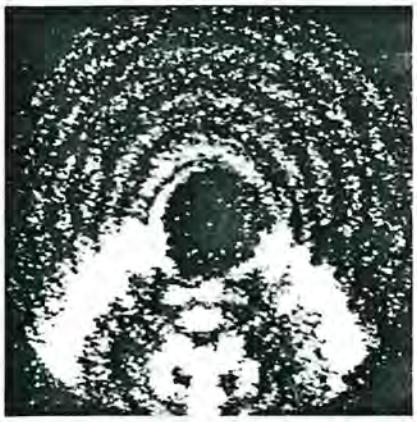

Fig. 9. Scattering pattern and image of a 16-μm-diameter oleic acid droplet containing an inclusion with greater size (relative to the host droplet) than that shown in Fig. 8.

the inclusion and the host, as is the case with water and oleic acid (0.998 g/cm^3 compared with 0.895 g/cm^3). The higher density water inclusion moves toward the top of the host oleic acid droplet when the droplet is accelerated downward within the airflow through the APS delivery nozzle.

These results are preliminary, and the exact mechanism by which the water inclusion is created is not yet known. One hypothesis is that water vapor condenses onto the original droplets and dissolves into the alcohol that is present. Once the alcohol has evaporated, the water, which has a higher surface tension than oleic acid, forms a single droplet enveloped by the oleic acid. To model such a system thermodynamically is complex but has been the subject of recent research by other authors.[15,16] For smaller host droplet sizes, the secondary scattering becomes distorted to yield downward bright arms as shown in Fig. 9. Theoretical analysis[1] suggests that this change in scattering is commensurate with an increase in the size of the inclusion relative to the host.

6. Discussion

The experimental data presented in this paper illustrate the complex spatial light-scattering behavior of droplets distorted by accelerating flow fields and droplets containing inclusions. To our knowledge, these data are the first of their type to be reported. The reproducibility of the experimental data makes them a valuable resource in the development and testing of theoretical inversion models. Such models may ultimately provide a route to the rapid characterization and identification of complex droplet morphologies, and this in turn could lead to advances in instrumentation for droplet aerodynamic sizing and for the detection of potential bioaerosol hazards in hospital and battlefield situations. In part II of this paper, numerically calculated spatial light-scattering data are presented which indicate that theoretical inversion of the light-scatter data is achievable for a variety of droplet morphologies that are relevant to the experimental conditions described above.

This research was carried out with funding from the UK Engineering and Physical Sciences Research Council (grant GR/L33375), the National Institute of Occupational Safety and Health, and with generous support from TSI Inc., St. Paul, Minn.

References

1. G. Videen, W. Sun, Q. Fu, D. R. Secker, R. S. Greenaway, P. H. Kaye, E. Hirst, and D. Bartley, "Light scattering from deformed droplets and droplets with inclusions. II. Theoretical treatment," Appl. Opt. **39,** 5031–5039 (2000).
2. J. K. Agarwal and R. J. Remiarz, "Development of an aerodynamic particle size analyser," USDHEW-NIOSH Contract Rep. 210-80-0800 (National Institute for Occupational Safety and Health, Cincinnati, Ohio, 1981).
3. P. A. Baron, "Calibration and use of the Aerodynamic Particle Sizer (APS 3300)," Aerosol Sci. Technol. **5,** 55–67 (1986).
4. W. D. Griffiths, P. J. Iles, and N. P. Vaughan, "The behaviour of liquid droplets in an APS 3300," J. Aerosol Sci. **17,** 427–431 (1986).
5. S. Holler, Y. Pan, R. K. Chang, J. R. Bottiger, S. C. Hill, and D. B. Hillis, "Two-dimensional angular optical scattering for the characterization of airborne microparticles," Opt. Lett. **23,** 1489–1491 (1998).
6. E. Hirst, P. H. Kaye, and J. R. Guppy, "Light scattering from nonspherical airborne particles: theoretical and experimental comparisons," Appl. Opt. **33,** 7180–7187 (1994).
7. P. H. Kaye, K. Alexander-Buckley, E. Hirst, and S. Saunders, "A real-time monitoring system for airborne particle shape and size analysis," J. Geophys. Res. D **101,** 19215–19221 (1996).
8. P. H. Kaye, E. Hirst, and Z. Wang-Thomas, "Neural-network-based spatial light-scattering instrument for hazardous airborne fiber detection," Appl. Opt. **36,** 6149–6156 (1997).
9. K. Willeke and P. A. Baron, *Aerosol Measurement: Principles, Techniques, and Applications.* (Van Nostrand Reinhold, New York, 1993).
10. W. J. Smith, *Modern Optical Engineering,* (McGraw-Hill, New York, 1966), pp. 439–443.
11. G. Ananth and J. C. Wilson, "Theoretical analysis of the performance of the TSI Aerodynamic Particle Sizer," Aerosol Sci. Technol. **9,** 189–199 (1988).
12. C. F. Bohren and D. R. Huffman, *Absorption and Scattering of Light by Small Particles* (Wiley-InterScience, New York, 1983).
13. The Mathworks, Inc. Matlab, 5.3.0.10183 (R11) (The Mathworks, Inc., 3 Apple Drive, Natick, Mass. 01760, 1999).
14. D. L. Bartley, A. B. Martinez, P. A. Baron, D. R. Secker, and E. Hirst, "Droplet distortion in accelerating flow," J. Aerosol Sci. (to be published).
15. T. Vesala, M. Kulmala, R. Rudolf, A. Vrtala, and P. E. Wagner, "Models for condensational growth and evaporation of binary aerosol particles," J. Aerosol Sci. **28,** 565–598 (1997).
16. T. Mattila, M. Kulmala, and T. Vesala, "On the condensational growth of a multicomponent droplet," J. Aerosol Sci. **28,** 553–564 (1997).